

# Development of boron-enhanced inconel 718 with superior thermomechanical properties for high-temperature concentrated solar power applications



Jeongwoo Lee<sup>a</sup>, Mathew Farias<sup>b</sup>, Hernan Aparicio<sup>a</sup>, Haomin Li<sup>c</sup>, Bardia Nabavi<sup>b</sup>, Bo Zhao<sup>b</sup>, Farid Ahmed<sup>a</sup>, Peiwen Li<sup>c</sup>, Ben Xu<sup>b,\*</sup>, Jianzhi Li<sup>a,\*\*</sup>

<sup>a</sup> Department of Manufacturing and Industrial Engineering, University of Texas Rio Grande Valley, Edinburg, TX, 78539, USA

<sup>b</sup> Department of Mechanical and Aerospace Engineering, University of Houston, Houston, TX, 77204, USA

<sup>c</sup> Department of Aerospace and Mechanical Engineering, University of Arizona, Tucson, AZ, 85721, USA

## ARTICLE INFO

### Keywords:

Additive Manufacturing (AM)  
Laser Powder Bed Fusion (LPBF)  
Inconel 718  
Boron  
Concentrated Solar Power (CSP)  
Solar Tower  
Solar Receiver Tube  
Heat Treatment

## ABSTRACT

This study presents the characteristics of a modified boron-enhanced Inconel 718 for elevated mechanical strength and excellent optical properties for the next generation of solar receiver tube applications. While the standard in industry to produce high absorptive surfaces is through utilizing coatings, it becomes more challenging to maintain for high-temperature applications ( $>800^{\circ}\text{C}$ ) for a long duration. The present study intends to directly increase the absorptivity of the Inconel 718 and bypass the need for coatings via Additive Manufacturing (AM) using boron-enhanced Inconel 718 powders. The effects of post-heat treatment and thermal cycling on microstructure, mechanical, and optical properties were analyzed systematically. The laser powder bed fusion (LPBF) technique enabled the boron content in Inconel 718 to increase up to 5000 ppm without microstructural defects (i.e., process defects). Increased boron content induced a larger amount of eutectic  $\gamma$  phase (involving Laves phases) development, leading to enhanced tensile strength and microhardness. Furthermore, it is observed that after heat treatment and thermal cycling, with high boron concentration the Laves phase morphology changed to a more interconnecting web-like structure. Thus, it is important to study the possible concentration of boron that can be added to the alloy using the LPBF process. A specially designed post-heat treatment was applied to remove the Laves phase with a long-striped shape and produce a smaller, granular-shaped Laves phase. Compared to pure Inconel 718, the boron-enhanced Inconel 718 showed that its microhardness increased to 36.6 % at the as-printed stage and up to 9.2 % after a proper heat treatment. Boron-doped Inconel 718 altered the optical properties by demonstrating that reflectance decreased by 10 %. This approach could lead to the development of more resilient and high-performance receiver tubes capable of withstanding extreme operating conditions, reducing maintenance costs, and extending the lifespan of CSP components. This study aims to remove the reliance on coatings with limited lifetimes by directly increasing the absorptivity of the utilized alloy. It is expected that limiting downtime that would otherwise be utilized for recoating solar absorber tubes could provide a more reasonable return on investment after considering operational expenses.

## 1. Introduction

Concentrated solar power (CSP) technologies transform thermal radiation into high-temperature thermal energy for various applications (e.g., heating and cooling, processing heat, material processing, electricity production, and chemical processes) [1]. The advantageous features of CSP technologies include almost zero greenhouse gas emissions,

high potential in lower production costs compared to photovoltaic, and higher flexibility in thermal energy storage (TES) [2–4].

Increasing the operating temperatures of heat transfer fluid (HTF) can enhance the thermal efficiency of a CSP system. Manzolini *et al.* [5] developed optimized hydraulic configurations and tube diameters of solar receivers that can operate at elevated temperatures up to  $715^{\circ}\text{C}$ , and their results showed that the levelized cost of energy (LCOE) could

\* Corresponding author.

\*\* Corresponding author.

E-mail addresses: [bxu12@central.uh.edu](mailto:bxu12@central.uh.edu) (B. Xu), [jianzhi.li@utrgv.edu](mailto:jianzhi.li@utrgv.edu) (J. Li).

potentially be lowered to \$151/MWh while the US Department of Energy's Sunshot initiative is aiming to a \$30/MWh or \$0.03/kWh [6]. Parabolic trough CSP systems typically operate at temperatures ranging from 300 °C to 400 °C, while molten salt-based solar tower CSP systems can achieve temperatures between 500 °C and 700 °C [7].

In solar tower CSP plants, the receiver is a critical component exposed to extreme operating conditions, which can significantly limit its lifespan [8–10]. Therefore, selecting appropriate materials is crucial for developing high-temperature CSP systems. For tubular receivers operating with temperatures above 700°C, the major technical challenges include: 1) severe tube deformation and fatigue due to uneven heat flux distribution and cyclic thermal stresses [11–14]; 2) tube corrosion caused by the molten salt at high temperature [15]; 3) cracks in the tube connecting zones due to thermal expansion and fatigue creep [5]. A solar receiver may have extreme thermal-mechanical loads on the structure due to high peak fluxes (more than 1000 suns) [16]. Accumulated thermal-mechanical loads resulting from repeated operations over a long time (months and years) can cause serious damage to the solar receiver. Additionally, corrosion from molten salt HTF can compromise the component's lifetime due to alloy oxidation and dissolution [16]. Fig. 1 (a) is an example of a concentrated solar tower, which involves a solar collector tube arranged in a circular design. The tubes are not heated uniformly, as they are typically heated from one side. Thus, the thermal gradient can lead to high strain and significant uneven deformation in the solar tubes, as shown in Fig. 1 (b) and (c). This behavior could be catastrophic for operations in the long term, resulting in large downtimes for maintenance. To address such issues, we suggest two approaches: (1) the investigation of an outstanding material that can withstand extreme environmental conditions (i.e., thermal cycling and corrosion), and (2) the consideration of a novel structure that can alleviate non-uniform heat accumulation.

First, the material for the next generation solar receiver needs to be carefully designed. An ideal solar receiver tube material should possess (1) strong mechanical properties under cyclic high-temperature conditions and (2) excellent high-temperature corrosion resistance to heat transfer fluids (HTF) [20,21]. Nickel-based superalloys have emerged as leading candidates for such applications due to their exceptional high-temperature strength, corrosion resistance, oxidation resistance, and ability to withstand extreme thermal and mechanical stresses [15, 22]. Because of such advantages, many studies have investigated characteristics and potential suitability of solar receiver tubes made of nickel super alloys: Inconel 718, Inconel 625, alloy 316H, Haynes 230, Inconel 625, Inconel 740H, and Incoloy 800H [18,23–30].

Second, the structural design of solar receiver tubes requires

improvement. The current design allows a high level of concentrated heat accumulation, leading to cyclic stress loading and severe deformation. Solar receiver tubes with a fin structure have gained attention because they can alleviate uneven solar flux loading by enhancing heat transfer within the CSP receiver tubes [31,32]. In particular, the swirl-inducing helical fin design is a promising candidate due to its effectiveness in suppressing non-uniform heat accumulation and enhancing structural and thermal performance [18,33,34].

The major challenges regarding the proposed solution lie in the low machinability of nickel super alloy and the high cost stemming from the complex 3D design. Laser-based additive manufacturing is a promising solution to the problem as it can synthesize metal alloys in complex 3D structures with a defect-free microstructure. Studies have demonstrated that a fully homogenized chemical composition can be achieved by optimizing process parameters (e.g., laser power, scan speed, powder feed rate) for steels [35,36], nickel-titanium alloys [37–39], titanium alloys [40,41], nickel alloys [42,43], aluminum alloys [44,45], and tungsten alloys [46,47]. One of the best advantages of such a method is that arbitrary target composition can be achieved through laser melting by controlling the chemical composition of the feedstock powders. Examples of developing new/adjusted alloy compositions using laser-based additive manufacturing techniques include high entropy alloys (HEA) [48,49] and minor adjustments to the target element composition in existing alloys [37,50]. In a similar manner, this technique can be utilized to synthesize the target material, Inconel 718 [51, 52].

In this study, for the development of outstanding solar absorber tube material, the authors investigated the feasibility of enhancing the material properties of Inconel 718 by adding a minor element, boron, in a laser-based additive manufacturing technique - laser powder bed fusion (LPBF). The LPBF technique has already demonstrated outstanding performances in manufacturing Inconel 718 with stabilized microstructure and mechanical properties compared to its counterpart, traditionally manufactured Inconel 718. On the other hand, there is a lack of data on other nickel superalloys manufactured via the LPBF technique. While some other nickel superalloys exhibit better high temperature and corrosion characteristics compared to Inconel 718, this study used Inconel 718 to receive the full benefit from a well-established powder provider and processing parameters. Adding minor elements into the superalloy system is an effective way to improve the material properties of superalloys. Boron is a well-known grain boundary-strengthening element [53] with many benefits. A small amount of boron doping can enhance the creep life and crack propagation resistance of some superalloys [54]. Adding boron enhances interface

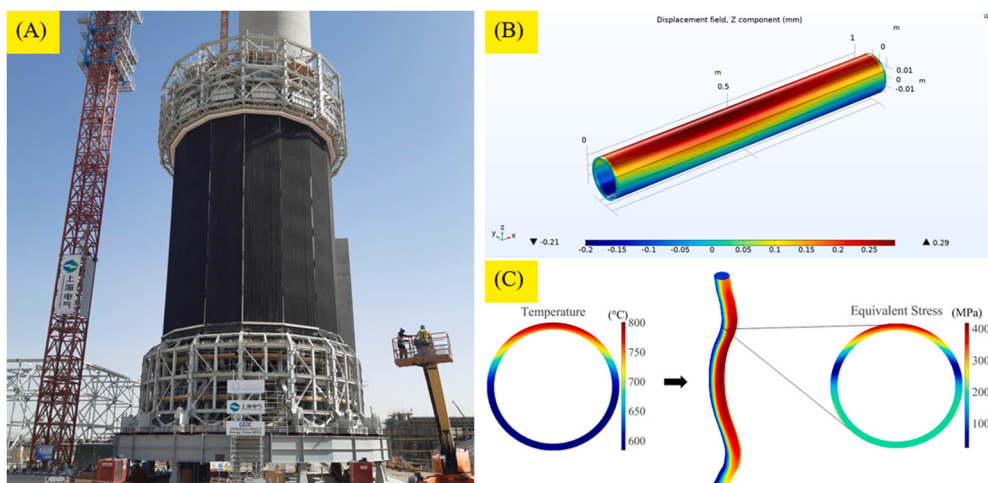


**Fig. 1.** (A) Tubular Receiver in a solar tower CSP system in Dubai [17]; (B) Deformation of a smooth solar receiver tube with uneven solar flux [18]; (C) Deflection and stress distribution in a solar receiver [19].

cohesion by forming strong covalent bonds [55,56] and filling void-type defects near the grain boundary [56]. The effect of boron is also known to include increasing hardenability (by achieving non-equilibrium boron segregation at grain boundaries), austenite recrystallization, and strain-induced precipitation [57].

While adding boron has advantageous effects on material properties, controlling the composition of boron is challenging, as an excessive amount of boron was reported to result in the degradation of mechanical properties. Zhou *et al.* [56] showed that the stress-rupture life of a nickel-based superalloy increased as boron content increased to 0.024 %, but the stress-rupture life decreased as boron content increased further. Yan *et al.* [58] showed that the ultimate tensile strength of nickel-based superalloy at high temperatures (870 °C) increased as boron content increased up to 70 ppm. Further increasing the boron content to 210 ppm decreased the ultimate tensile strength. Xiao *et al.* [59] reported that low-cycle fatigue (LCF) of IN718 increased while boron concentration changed from 12 ppm to 60 ppm, but the LCF decreased when boron concentration increased from 60 ppm to 100 ppm. Similarly, using fractographic analysis, Xiao *et al.* [60] investigated the number of cracks in Inconel 718. It was observed that the number of cracks decreased as the boron concentration changed from 12 ppm to 60 ppm, but the number of cracks increased as the boron concentration increased from 60 ppm to 100 ppm.

This study focused on investigating enhanced material properties of Inconel 718 with its boron content beyond the conventional limit of ~100 ppm. The new limit of boron content through the LPBF technique was explored by increasing the boron content up to 10,000 ppm. Detailed mechanical properties and microstructure of boron-added Inconel 718 were analyzed in different manufacturing stages: (1) as printed, (2) after heat treatment, and (3) after thermal cycling, which

mimics the realistic operational condition of the solar receiver. Moreover, the optical performance of the new material was analyzed by measuring the reflectivity and emissivity at the surface, which is directly linked to solar energy harvesting efficiency. This study aims to remove the reliance on coatings with limited lifetimes by directly increasing the absorptivity and decreasing the emissivity of the utilized alloy in the visible light range while minimizing the emissivity of the alloy in the infrared range. While it may prove too difficult to manage both aspects regarding the increased lifetime of solar receiver tubes, it could provide a reasonable return on investment after considering operational expenses, provided parts need less maintenance.

## 2. Design of experiments

### 2.1. Material and manufacturing process design

**Fig. 2** shows the material designs and the associated manufacturing process. A new material composition of Inconel 718 and Boron was designed to achieve better performance (i.e., high solar absorptivity) and reduce the need for recurring maintenance for the solar receiver tube application. The manufacturing process includes powder mixture preparation, laser powder bed fusion technique, and post-heat treatment.

#### 2.1.1. Powder mixture preparation

Inconel 718 (EOS NickelAlloy IN718) and boron (Chemsavers) powders were used in this study. All powers were sieved into the size range of 50–150 µm before mixing. The powder mixture ratio was carefully controlled by measuring weights of Inconel 718 and boron powders to achieve following compositions: (1) Pure Inconel 718, (2)

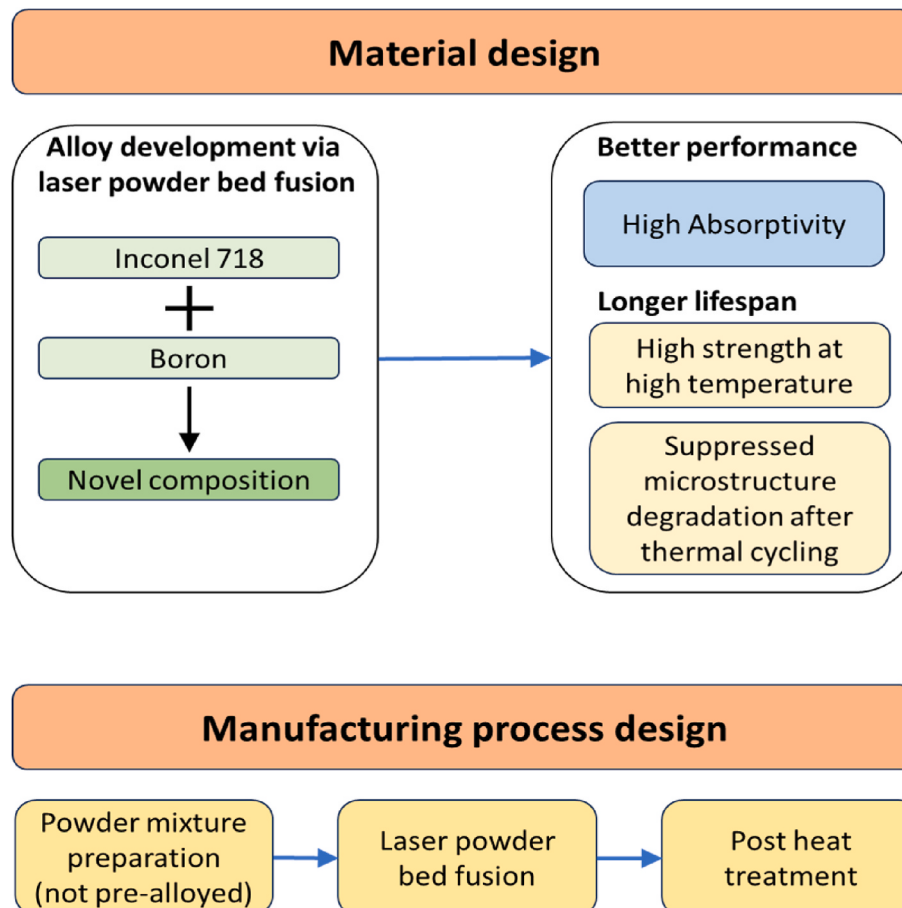


**Fig. 2.** Material design and manufacturing process design.

boron 500 ppm (0.05 wt%), (3) boron 1000 ppm (0.1 wt%), (4) boron 5000 ppm (0.5 wt%), and (5) boron 10,000 ppm (1.0 wt%). Powder mixtures were blended using a V-type powder mixer (Capsulcn V-5 V-type mixer) for 24 h. In this study, samples were named S1, S2, S3, S4, and S5 based on their composition, as shown in Table 1.

### 2.1.2. Laser powder bed fusion process

The 5 sample compositions in Table 1 were produced using an EOS M290 Laser Powder Bed Fusion system. The equipment features a 400-W Yb-fiber laser operating at a continuous wave of 1070 nm. The samples were constructed on pre-heated wrought Inconel 718 substrates at 80°C. To distribute the powder mixture of Inconel 718 and boron, the system uses a steel recoater blade. Details regarding the laser scanning parameters can be found in Table 2. The printing process took place in a chamber filled with Argon, and the oxygen levels were maintained at 0.1 % to prevent oxidation during fabrication.

### 2.1.3. Post-heat treatment and thermal cycling

Post-heat treatment and thermal cycling conditions used in this study are shown in Fig. 3. The post-heat treatment condition was selected to improve microstructure in terms of homogeneity and strength enhancement [61]. As for post-heat treatment and thermal cycling, a Paragon Sentry Xpress 4.0 furnace was used. The heating rate was maintained at 5 °C/min while the furnace cooling (FC) was applied to the cooling procedure. All post-heat treatment and thermal cycling procedures were conducted under ambient conditions.

## 2.2. Microstructural analysis

All samples were sectioned using a PACE Technologies MEGA-T250S wet saw and polished for further analysis. The rough surface polishing procedure started with silica abrasive papers with 320 grit and gradually decreased to 400, 600, and 800 grits. Sample surfaces were subsequently fine polished starting from 15 µm diamond paste, followed by 0.05 µm colloidal silica.

Grain structure was investigated using a scanning electron microscope (SEM) JSM-7100F (JEOL). Detailed elemental compositions of spots and regions on the sample surface were analyzed by energy dispersive X-ray analysis (EDAX) with an accuracy within ±2 %. X-ray diffraction (XRD) analysis was conducted to study the phase composition of manufactured samples using Bruker D8 Advance equipped with a CuK $\alpha$  X-ray source. The 2θ scanning range from 30° to 90° at a rate of 5°/min was used for XRD analysis.

## 2.3. Mechanical property analysis

Microhardness and tensile properties of samples were measured at room temperature in the atmospheric environment. Microhardness measurement was conducted using the microhardness tester (Shimadzu HMV-G). The diamond indent was applied to the sample surface with a 500 g load for 15 s. Tensile testing was conducted on samples prepared in dog-bone shape following ASTM E8 standard (rectangular tension test specimens). The strain rate of 0.001/s was applied while strain was measured by an extensometer until failure.

**Table 1**  
Compositions of samples in this study.

Sample Name	Composition
S1	Pure Inconel 718
S2	Boron-enhanced Inconel 718 (boron: 500 ppm, 0.05 wt%)
S3	Boron-enhanced Inconel 718 (boron: 1000 ppm, 0.1 wt%)
S4	Boron-enhanced Inconel 718 (boron: 5000 ppm, 0.5 wt%)
S5	Boron-enhanced Inconel 718 (boron: 10,000 ppm, 1.0 wt%)

**Table 2**  
Laser operating parameters of the LPBF process.

Parameter	Value
Laser power	285 W
Scanning speed	960 mm/s
Hatch distance	0.11 mm
Layer thickness	0.05 mm
Substrate	Inconel 718
Hatch strategy	10 mm Stripes

## 2.4. Optical property analysis

While reflectance is largely recorded using directional beams, in this case at a near normal incident angle, the rough surfaces inherent in the LPBF process tend to produce diffuse reflections. Reflected rays are scattered in many directions, causing the directional reflectivity to yield much lower than what is realistic. To remedy this issue, an integration sphere was used to measure the directional hemispherical reflectivity near the normal direction. As the wavelength range spans upwards to the Near Infrared (NIR) and Infrared (IR), measurements for reflectance in the visible light range can readily be measured using a spectrophotometer, but longer wavelengths in NIR require separate measurements using a Fourier Transform Infrared (FTIR) spectrometer. For the IR and NIR light range, the Thermo Fisher iS50 FTIR spectrometer was utilized to perform reflectance measurements spanning the 1500–5000 nm range. A KBr beam splitter was utilized with a DTGS detector in all measurements. The FTIR and the gold-coated integrating sphere were calibrated using a gold sample, and NIR measurements were taken in strict 2-hour time frames between calibrations to account for changes in humidity and/or temperature in the room. The samples completely covered the aperture opening to ensure that the reflectance is measured accurately. The Jasco V780 UV-VIS spectrophotometer with a polymer-coated integration sphere was used for measurements in the visible and limited NIR, ranging from 350 to 1600 nm.

## 2.5. High temperature optical properties

The FTIR was utilized with an emissometry setup proposed in Ref. [62] implementing the use of Instec HS1200G, a PID-controlled heating stage. Samples are heated up to 700 °C and the emitted beam are redirected through gold-plated mirrors to the FTIR to provide emissivity measurements. In this study, a black body was used to help determine the emissivity with Eq. (1):

$$\varepsilon(\lambda, \theta, T_s) = \varepsilon_R(\lambda) \frac{I_S(\lambda, \theta, T_s) - I_{BG}(\lambda, \theta, T_s)}{I_{BB}(\lambda, T_s) - I_{BG}(\lambda, \theta, T_s)} \quad (1)$$

where  $I_S$ ,  $I_{BG}$ , and  $I_{BB}$  represents the measured intensity from the sample, background, and blackbody.  $T_s$  is the temperature of the sample,  $\lambda$  is wavelength and  $\theta$  is angle of emission which is set as normal angle.  $\varepsilon_R$  is the reference emissivity which is unity regarding to blackbody. Samples were fixed to a heat source using thermal tape, and external surface temperatures were confirmed 700 °C with an attached K-type thermocouple mounted to the exposed surface. Blackbody is maintained at the same temperature with sample to ensure accurate spectral emissometry.

The high-temperature emissometry setup is exposed to the environment. This limitation of the current apparatus prevents the use of an integration sphere to study the total hemispherical emissivity.

## 2.6. Surface property analysis

The Keyence VK-X3000 surface profilometer was used to measure and calculate both the surface area roughness and line roughness parameters. It was also utilized to generate topographical maps of the surfaces parallel to the build direction. Considering that all samples were at some point cut from the substrate, it is important to set the

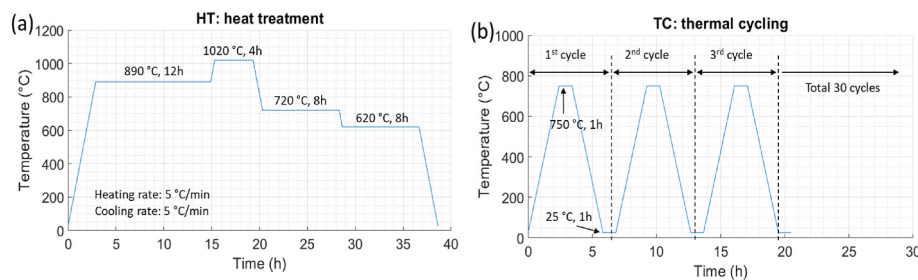


**Fig. 3.** (a) Heat treatment (HT), and (b) thermal cycling (TC) conditions.

reference plane to the average of the surface in case a cut renders a sample no longer level on the profilometer as this would cause issues in the calculation of the surface roughness. The VK-X3000 was utilized to re-level all data, as surface roughness measurements are subject to peak-to-peak measurements, and this change is insignificant in the final data. This re-leveling is applied uniformly to all images and normalized to the largest peak-to-peak range. All surface roughness areas were selected as a 1900  $\mu\text{m}$  square area that encompassed the center region of the scanned surface. Using the VK-X3000 software, the measurements were done in a single batch to ensure that they were consistent. No filters were applied to the measurements, while it was considered to use the high-pass L-filter, it was determined that this might remove large-scale

features, such as the waviness inherent to the layer-by-layer build process.

### 3. Results

#### 3.1. Microstructure and mechanical properties

##### 3.1.1. Limitations of boron content of Inconel 718

The maximum allowance of boron content in Inconel 718 was studied by gradually increasing the boron content in samples using the LPBF technique. Cube and disk samples were prepared on Inconel 718 substrate, as shown in Fig. 4. Samples with different compositions (S1-

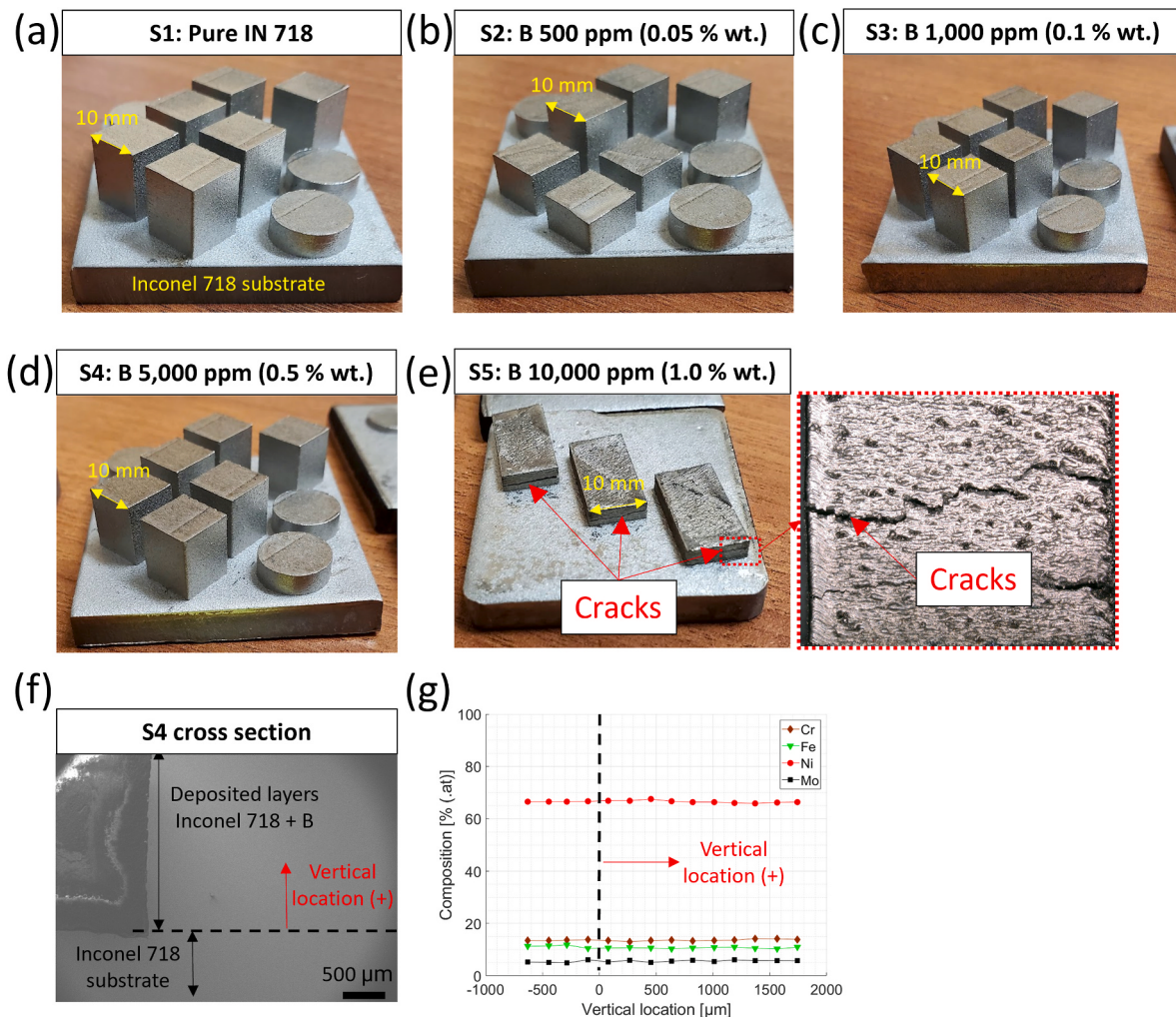


**Fig. 4.** Samples in as-printed state (a) S1: pure Inconel 718, (b–e) S2–S5: Inconel 718 with enhanced boron composition ranging from 500 ppm to 10,000 ppm, (f) Cross section SEM image and EDAX data of S4 sample surface.

S5) were deposited using the same operating parameters as shown in **Table 1**. It should be noticed that samples with boron contents less than 5000 ppm (S1 – S4) achieved stable layer deposition, leading to the final structure (10 mm cube) without cracks, as shown in **Fig. 4(a-d)**. On the other hand, the sample with a boron composition of 10,000 ppm (S5) experienced layer delamination during the LPBF process, which led to severe crack formation, as shown in **Fig. 4(e)**. The results indicate that the maximum boron allowance for Inconel 718 is between 5000 ppm and 10,000 ppm in the LPBF process. A cross-sectional analysis investigated micro defects on other samples with boron contents less than 5000 ppm (S1 – S4), as shown in **Fig. 4(f)**. Defect-free microstructures were observed in all samples, which indicated successful fusion of Inconel 718 and boron powder particles. **Fig. 4(g)** shows EDAX data along the vertical direction in **Fig. 4(f)**. SEM and EDAX results indicate that the same matrix phase with stable chemical composition was formed at the printed layers compared to the substrate material.

The effect of boron content in Inconel 718 was investigated by detailed microstructure analysis through SEM and XRD, as shown in **Fig. 5**. Detailed EDAX analysis results for major phases are shown in **Appendix A**. According to SEM images, **Fig. 5(a-d)**, the major effect of increasing boron content on the microstructure was a gradual change in the shape and density of the interdendrite  $\gamma$  phase. The term “interdendrite  $\gamma$  phase”, which indicates a compound composed of eutectic  $\gamma$  and Laves phase, has been used for the additively manufactured Inconel 718 microstructure [61,63]. According to the EDAX result (**Fig. A.1** and **Table A.1**), the main difference between the matrix  $\gamma$  phase and the interdendrite  $\gamma$  phase is the amount of detected Nb element. The Nb content in this study in the as-printed stage was 6.51 (wt. %), which is in good agreement with that of interdendrite 4.3 (wt. %), considering the  $\pm 2\%$  tolerance in the EDAX analysis. The amount of interdendrite  $\gamma$  phase increased to 13.4 % and 29.7 % as boron content increased to 1000 ppm and 5000 ppm, respectively. The shape of the interdendrite  $\gamma$  phase changed from a small granular shape (0.2–0.3  $\mu\text{m}$ ) to an elliptical shape (0.6–1.7  $\mu\text{m}$ ), and a connected web shape.

In this study, the Laves phase was not detected in the as-printed stage, regardless of boron content, through either SEM or XRD analysis, despite the Laves phase being commonly present in additively manufactured Inconel 718 [64,65]. While the Laves phase was not clearly visible in SEM images and was not detected in XRD results, it was

claimed that the Laves phase always appears at the interdendrite area [61]. Liu *et al.* [66] reported that a similar microstructure (core dendrite and interdendrite) was achieved using the laser solid forming (LSF) technique, while no Laves phase peaks were observed in the XRD result. The missing XRD Laves peak was explained by the following reasons: (1) the volume fraction of Laves was too low, and (2) the diffraction peaks of Laves were too low compared to the strong-oriented  $\gamma$  dendrite diffraction peaks. Due to the presence of a high amount of interdendrite  $\gamma$  phase, the S4 sample is expected to show the lowest plasticity [67] among all samples.

Regardless of boron contents, all samples (S1-S4) showed chemically stable layer deposition achieved during the LPBF process according to EDAX analysis results (elements of Cr, Fe, Ni, and Mo). According to XRD analysis, as shown in **Fig. 5(e)**, whereas **Fig. 5(a-d)** indicates the locations where the XRD analysis was conducted on the samples, all samples showed the same phase peaks regardless of their boron contents. While studies claim that  $\gamma''$  phase (D0<sub>22</sub>-ordered Ni<sub>3</sub>Nb) shares the same XRD peak as  $\gamma$  and  $\gamma'$  which are located at 20 angles from 40° to 60° [68–72],  $\gamma''$  was determined not to be present in the as-printed stage because the  $\gamma''$  phase was clearly visible in the heat-treated stages in this study. Since the primary objective of this study was to investigate the feasibility of the boron-enhanced Inconel 718, an in-depth microstructural study (e.g., TEM) was not performed and is planned for future work.

### 3.2. Effects of heat treatment and thermal cycling

#### 3.2.1. Microstructure and mechanical properties

The effect of heat treatment (HT) was studied using SEM images, as shown in **Fig. 6**. After the same HT, samples with different boron contents revealed different microstructures. Based on the EDAX result (**Fig. A.1** and **Table A.1**), a new phase with high Nb content appeared in all samples. In this study, the Nb-rich phase is concluded to be Laves because of the following reasons. First, the new phase showed high Nb content and similar Cr content compared to the  $\gamma$  matrix, which is characteristic of the Laves phase [73]. In contrast, another common Nb-rich phase, NbC, is composed of much lower Cr content (less than 2 wt %), thus ruled out. Second, the large amount and the large size of the new Nb-rich phase in sample S4 indicate that it originated from the base material with large Nb-rich sites. As shown in **Fig. 5(d)**, the S4 sample

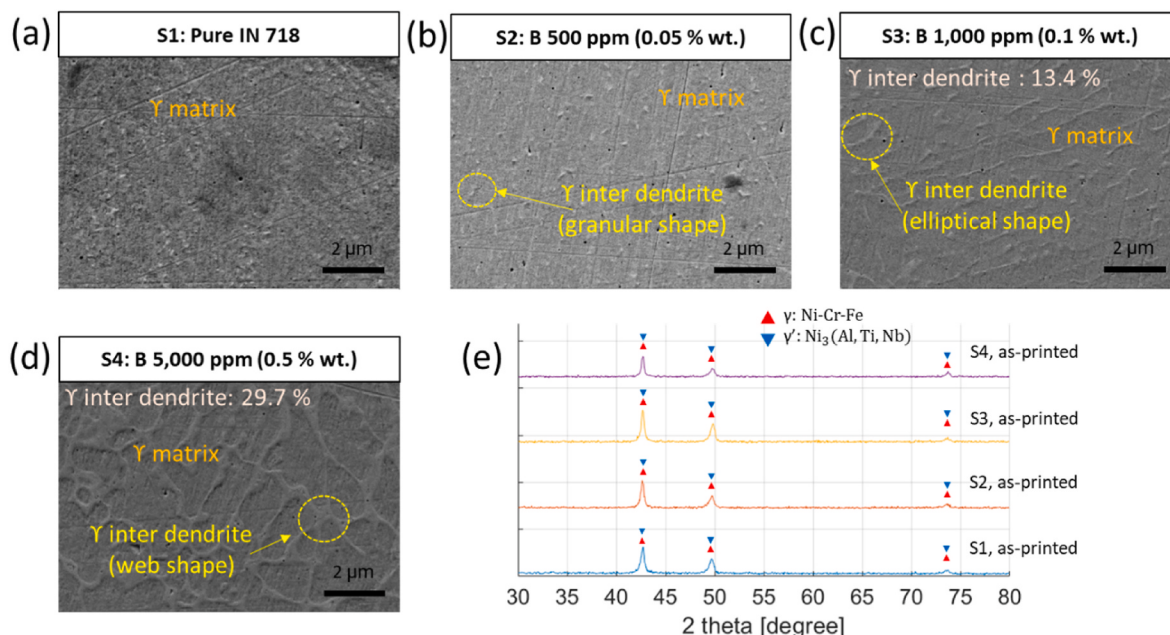


**Fig. 5.** (a-d) SEM images of samples (S1-S4) in as-printed state (e) XRD results of S1-S4 samples.

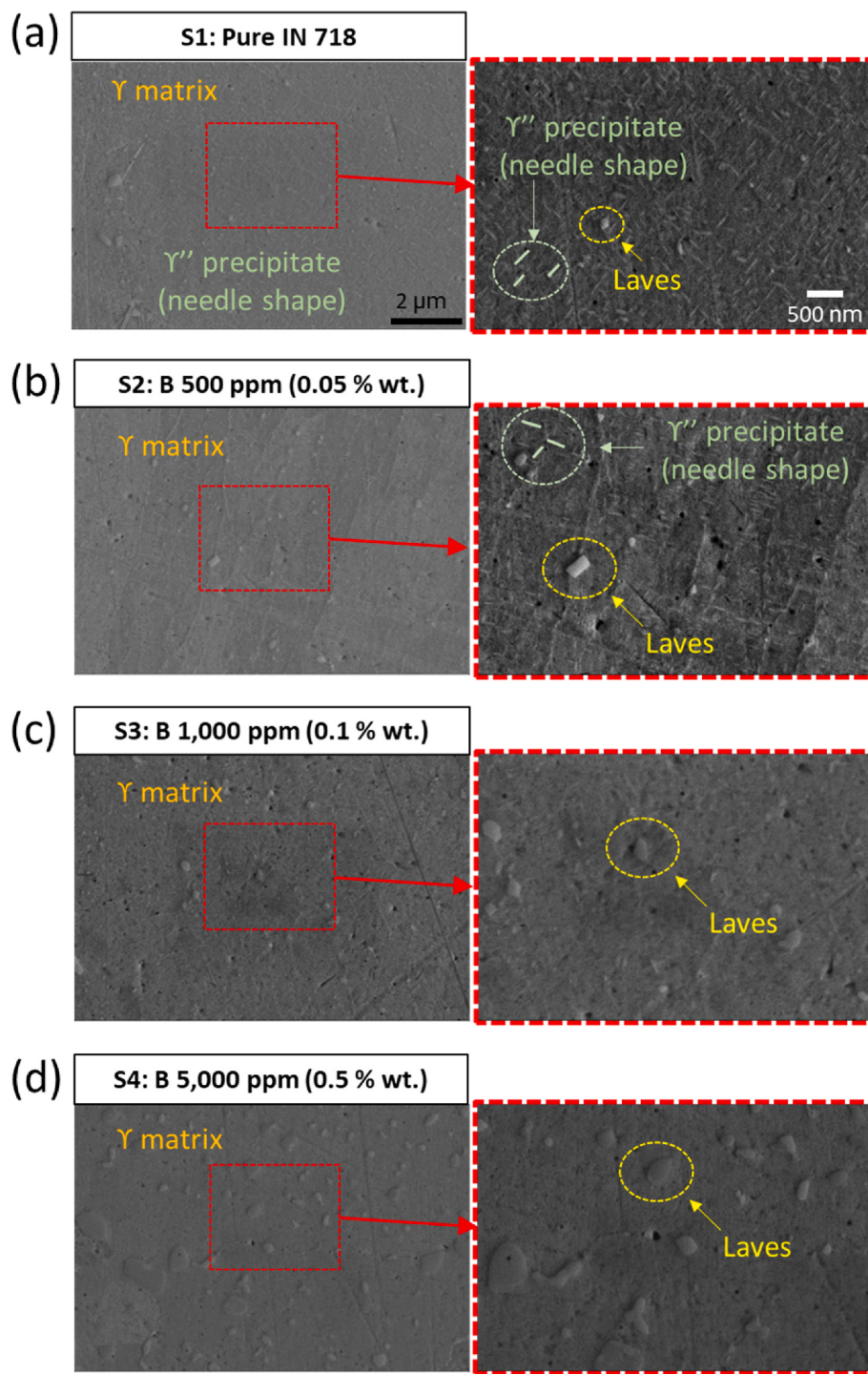


**Fig. 6.** (a-d) SEM images of samples (S1-S4) after heat treatment (HT) state.

showed a large area of interdendrite  $\gamma$  phase with high Nb content. Lastly, the heat treatment condition was designed to segment the Nb-rich phase (interdendrite  $\gamma$  phase) by inducing a needle-shaped  $\delta$  phase within it. As designed, the large web-shaped interdendrite  $\gamma$  phase was successfully cut into smaller Laves phase as reported by Liu *et al.* [61]. As discussed in the previous section, a more in-depth microstructural study, including Transmission Electron Microscopy (TEM) analysis, is planned for further work to provide precise phase composition.

While the Laves phase was observed in all samples, only samples with relatively lower boron contents (S1 and S2) showed clear precipitation of lenticular and disc-shaped (oblate spheroid)  $\gamma''$  phase [74]. Both

the Laves phase and the  $\gamma''$  phase are composed of high Nb [61,75] and evolved from the area of the eutectic  $\gamma$  phase where Nb content is sufficient [61]. As boron content increased above 1000 ppm, samples S3 and S4 showed suppressed formation of  $\gamma''$  precipitate and an increase in Laves phase. As designed, the heat treatment process (HT) successfully produced granular-shaped Laves phases by cutting down the web-shaped or long-striped eutectic  $\gamma$  phase present in the as-printed stage.

The result indicates that the final microstructure (size and composition ratio among  $\gamma$ ,  $\gamma''$ , and Laves) can be altered by controlling the boron content in Inconel 718. For high-temperature applications, such

as solar receiver tubes in this study, understanding the characteristics of the constituent phases is important for designing a desirable microstructure. It is well reported that the  $\gamma''$  phase is the resultant precipitate from double-aging heat treatment [76] and can enhance both the microhardness and tensile strength [67]. However, prolonged exposure to higher temperatures (above 650 °C) can transform the metastable  $\gamma''$  phase into a potentially deleterious  $\delta$ -phase [64]. The  $\delta$ -phase is reported as a potential crack source due to its sharp edges that can act as a crack initiator at high stresses [77]. The Laves phase is generally known to be detrimental to the material properties (tensile ductility, fatigue, and creep rupture) of Inconel 718 [78]. However, Sui *et al.* [79] showed that only Laves phases in long-striped shapes negatively affect the mechanical properties. In contrast, small granular-shaped Laves phases can benefit the plastic deformation of Inconel 718. Again, Fig. 6 showed that the HT process produced Laves phases in smaller granular shapes.

The comparison of the mechanical properties of samples before and after the HT process revealed the characteristics of the newly formed microstructure ( $\gamma''$  phase and Laves phase). Tensile stress-strain data of samples before and after the HT process are shown in Fig. 7. For as-printed samples, the amount and the shape of the  $\gamma$  eutectic phase mainly affected the tensile characteristics of the samples. Tensile strength was enhanced gradually as the amount of  $\gamma$  eutectic increased in the microstructure of samples (S1-S3). The ultimate strength values were observed as 1082.6 MPa, 1125.7 MPa, and 1149.1 MPa for samples S1, S2, and S3, respectively. On the contrary, the increased amount of the  $\gamma$  eutectic phase suppressed the ductility of the samples. The maximum elongation values were 34.2 %, 22.8 %, and 22.7 % for samples of S1, S2, and S3. It should be noted that the shape of  $\gamma$  eutectic phase changed from granular to elliptical, from S2 to S3, which increased the tensile strength while ductility was not affected. When the shape and the amount of  $\gamma$  eutectic changed into a dense web-shaped sample (S4), the sample achieved the highest tensile strength but failed before plastic deformation. The maximum strength and the maximum elongation for the sample S4 are 1078 MPa and 1.6 %, respectively.

Samples after the heat treatment process (HT) showed enhanced tensile strength of samples with decreased ductility. Due to the precipitation of  $\gamma''$  phase and the formation of the granular Laves phase, all samples except S4 showed increased ultimate tensile strength of 300–400 MPa. It should be noted that the S4 sample, after the HT process, achieved both higher strength and improved ductility. The result indicates that web-shaped  $\gamma$  eutectic (Fig. 5 (d)) is detrimental to tensile properties, while the presence of granular-shaped Laves phase (Fig. 6 (d)) enhances tensile strength. Also, the ductility of S4 was not severely impaired compared to that of S3 when the amount of granular-shaped Laves phase was increased from S3 to S4. The sample S3 achieved the highest ultimate tensile strength of 1460 MPa with an elongation of 12.5 %. Park *et al.* [80] reported the ultimate tensile strength of 1286 MPa

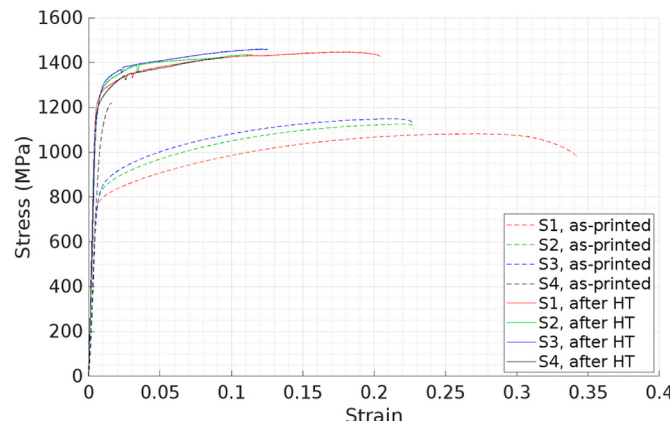


**Fig. 7.** Tensile stress-strain plot of samples before and after HT process.

with an elongation of 7.3 % from LPBF Inconel with similar post-heat treatment (solution + double aging).

Thermal cycling (30 cycles) of samples at 750 °C for 1 hour affected the microstructure differently according to their boron contents. SEM images and XRD results are shown in Fig. 8. It should be noticed that the sample with the highest boron content (S4) showed relatively dense and thicker web-shaped interdendritic eutectic  $\gamma$  phase compared to other samples (S1, S2, and S3). Also, the amount of carbide phase, which is reported as beneficial to mechanical properties [81], increased as boron content increased. The result indicates that ‘eutectic  $\gamma$  + carbide’ phase evolved from granular-shaped Laves phase in the previous ‘after HT’ stage microstructure (Fig. 6). Also, it was observed that the microstructure after HT + TC is largely affected by the initial boron composition of the material. The temperature of the TC process (750 °C) is close to the double aging process of Inconel 718 (720 °C/8 h + 620 °C/8 h), which induces precipitation of  $\gamma'$  and  $\gamma''$  phases [82]. However, the samples in this study showed the removal of  $\gamma''$  phases after the TC process with the reformation of the interdendritic eutectic  $\gamma$  phase. The result highlights the importance of boron content in controlling the final microstructure of Inconel 718 in the field application where thermal cycling is involved. To the authors’ best knowledge, the effect of repeated thermal cycling at 750 °C on microstructure has not been reported.

Boron-enhanced Inconel 718 demonstrated higher microhardness, as shown in Fig. 9. Compared to the pure Inconel 718, the microhardness of boron-enhanced Inconel 718 was increased up to 36.6 %, 9.2 %, and 19.0 % for as-printed, after HT, and after HT + TC when boron content was increased to 5000 ppm, respectively. For the as-printed samples, the microhardness increased from 298 HV to 407 HV as the boron content was increased to 5000 ppm. The result can be explained by the increased amount of eutectic  $\gamma$  phase (including Laves), which is reported to be hard and brittle [61]. An increasing trend was also observed from the after-HT and the after HT + TC stages. The microstructure hardening effect after HT is because of the precipitation of  $\gamma''$  phase and the formation of the granular Laves phase. After HT + TC, the increased amount of eutectic  $\gamma$  phase affected the increase in microhardness. It should be noted that an increasing trend was not observed in samples S3 and S4 after HT. The result indicates that the increased amount of granular Laves phase, only, did not affect the microhardness of the samples.

The increased microhardness of boron-enhanced Inconel 718 indicates that higher mechanical properties were achieved, which is necessary to withstand high thermal stress. However, due to the extreme thermal cycling conditions of the solar receiver tube, changes in both the microstructure and mechanical properties should be carefully considered. Considering a large difference in microhardness of S4 between the two stages, after HT and after HT + TC, it can be concluded that the TC process triggered the formation of a thicker eutectic  $\gamma$  phase. As shown in Fig. 7, a large amount of eutectic  $\gamma$  phase is detrimental to mechanical properties as the microstructure cannot withstand plastic deformation. Also, the solar absorber tube application requires microstructures that can withstand thermal cycling (TC) without severe changes. Thus, S4 should be excluded from consideration, while S3 should be appreciated because of the minimal change in microhardness between the two stages, after HT and after HT + TC.

### 3.2.2. Surface characteristics

Fig. 10 shows the as-printed surfaces and the surface roughness values for  $S_a$ ,  $S_z$ ,  $S_{pc}$ , and  $S_{ku}$ . Where  $S_a$  value indicates the arithmetical mean height roughness,  $S_z$  is the surface roughness as measured using the sum of the peak height and peak depth,  $S_{pc}$  is the arithmetic mean peak curvature, and  $S_{ku}$  is Kurtosis. In this analysis, a sizeable number of satellite particles have sintered onto the sample’s surface. Samples such as the 1000 ppm (S3) and 5000 ppm (S4) generally had lower surface roughness than the lower concentration 500 ppm (S2) and Pure Inconel

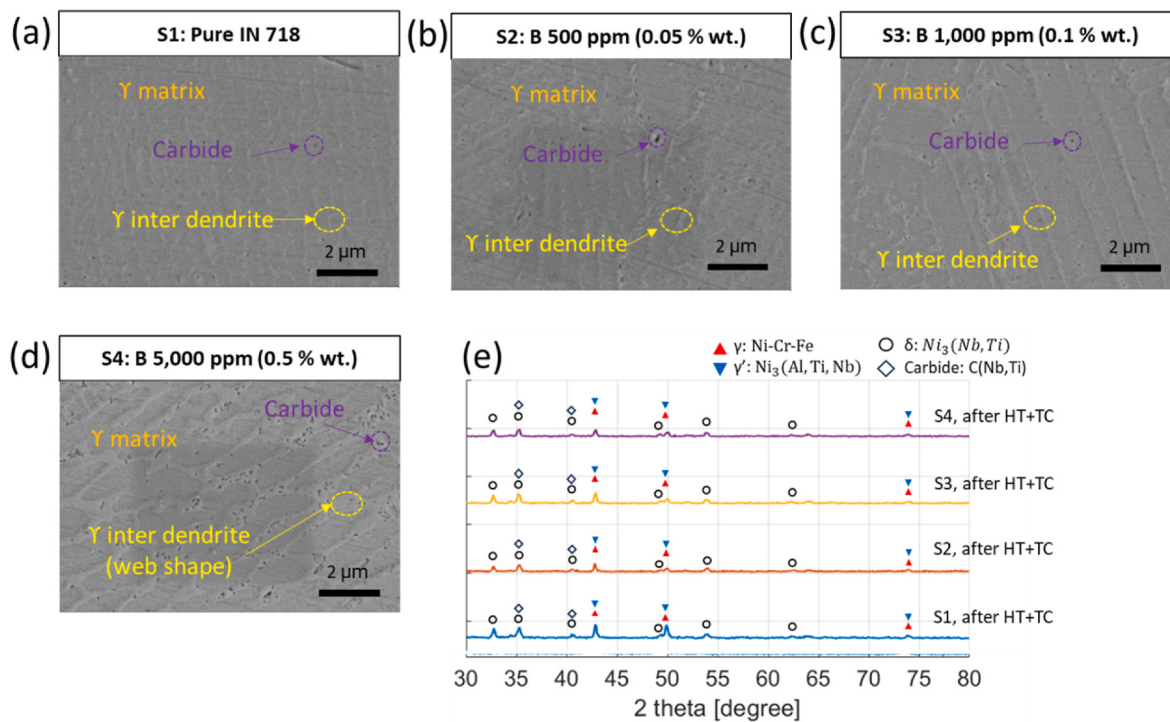


**Fig. 8.** (a-d) SEM images of samples (S1-S4) in after heat treatment (HT) and thermal cycling (TC) state (e) XRD results of S1-S4 samples.

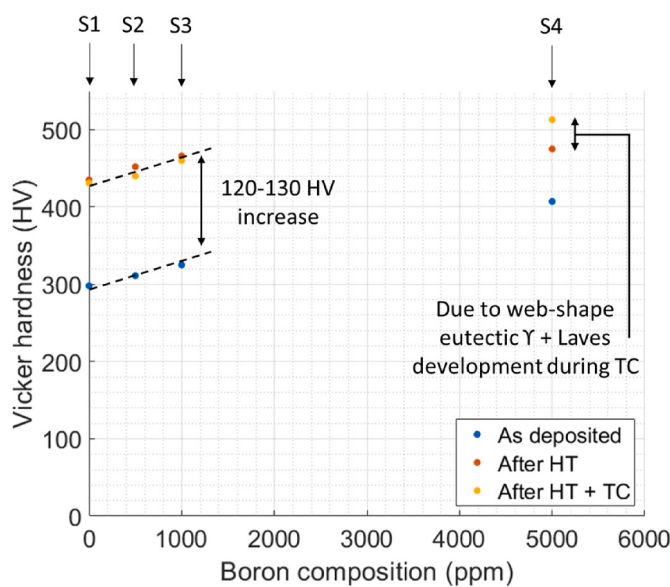


**Fig. 9.** Microhardness of samples at different heat treatment stages: as-deposited, after heat treatment (HT), and after heat treatment (HT) and thermal cycling (TC).

718 samples (S1). However, no clear trend presented itself in the Spc and Sku values. However, it should be noted that given the nature of LPBF printing, the shifts in these values might not be significant at this time. Furthermore, as these were printed in an inert environment and imaged shortly after, it is unlikely that they have undergone significant oxidation that would impact the as-printed surfaces. It can be suggested that, given the surface morphology, any change in material properties may be attributed to hardening from the addition of boron, which is likely caused by boride precipitates or grain boundary segregation. This behavior is believed to be exacerbated after HT + TC, as segregation to the grain boundaries can be facilitated during the HT + TC process.

**Fig. 11** shows the surface morphology of the previous samples after HT + TC. Some oxidation likely happened on all the surfaces during the heat treatment and thermal cycling, which is believed to have contributed to changing the surface morphology. Moreover, the Spc value is significantly higher in both the 500 ppm (S2) and pure Inconel 718 samples (S1), indicating that these samples had sharper features. In contrast, the higher-concentration samples had more rounded features; the high surface roughness and sharpness of the features could lead to some fatigue limitation, as well as the introduction of stress concentrations on the surface of the samples. This upward tick in the Spc value might be caused by oxidation during the HT + TC process. With lower Boron concentrations, it is possible that the alloy is more readily oxidized on the surface, while the high Boron concentration samples have a higher chance of oxidation on the grain boundaries as the boron segregates to the grain boundaries and forms Boron oxides. Both the grain boundary segregation and the formation of oxides could contribute to the strength as well as the hardening of the material, while significantly increasing the embrittlement of the material.

### 3.2.3. Solar reflectivity and absorptivity

**Fig. 12** compares Inconel 718 (S1) with varying boron concentrations of 500 ppm (S2), 1000 ppm (S3), and 5000 ppm (S4) under different conditions: as-printed and heat-treated with thermal cycling (HT + TC). In **Fig. 12**, the wavelengths denoted as  $\lambda_{cut 1}$  (1790 nm) and  $\lambda_{cut 2}$  (2400 nm) indicate the wavelength range of interest based on a study from Burlafinger [83]; where it is suggesting the ideal selective absorber, under the below concentration factors 120 and above 600 has an optical cutoff of 2400 nm, while the optimal cutoff for a concentration factor between 120 and 600 suns is 1790 nm. The visible light range maximum is marked at approximately 700 nm. The results indicate that a relatively high concentration of boron increases reflectance, with the highest concentration (5000 ppm) showing the most significant increase. Additionally, heat-treated samples exhibit distinct optical differences from their as-printed counterparts, particularly at longer wavelengths, suggesting that both boron addition and thermal cycling influence the material's optical properties.

Boron is believed to play a key role in refining the grain structure of

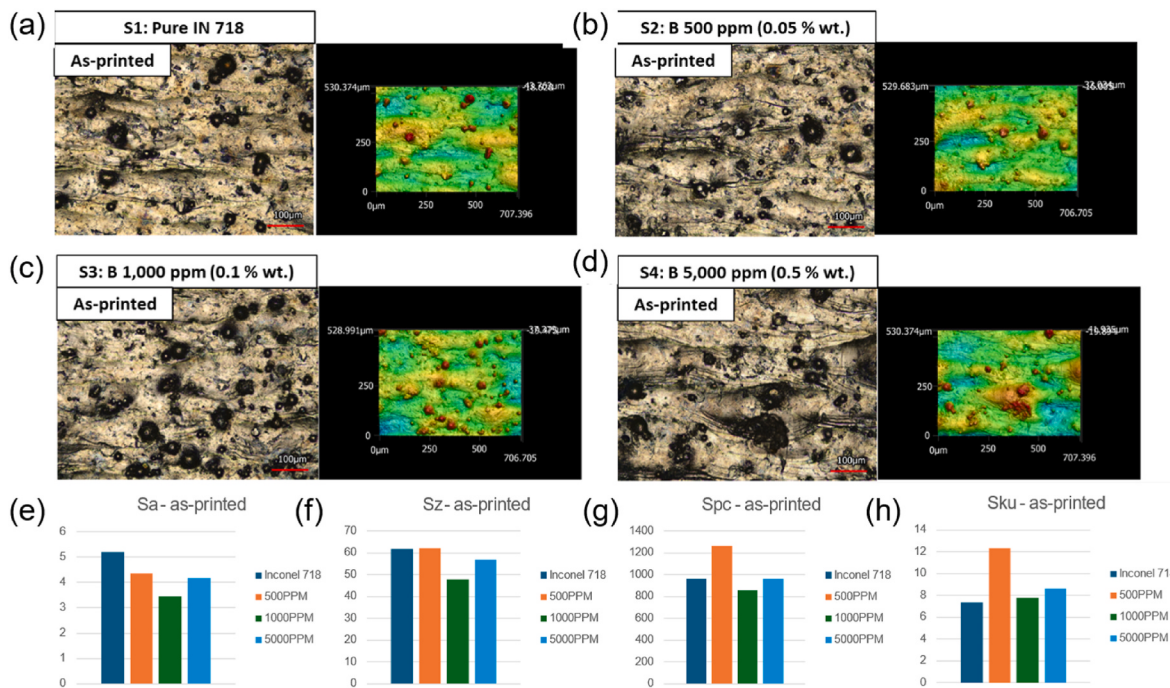


Fig. 10. Surface characteristics of as-deposited samples.

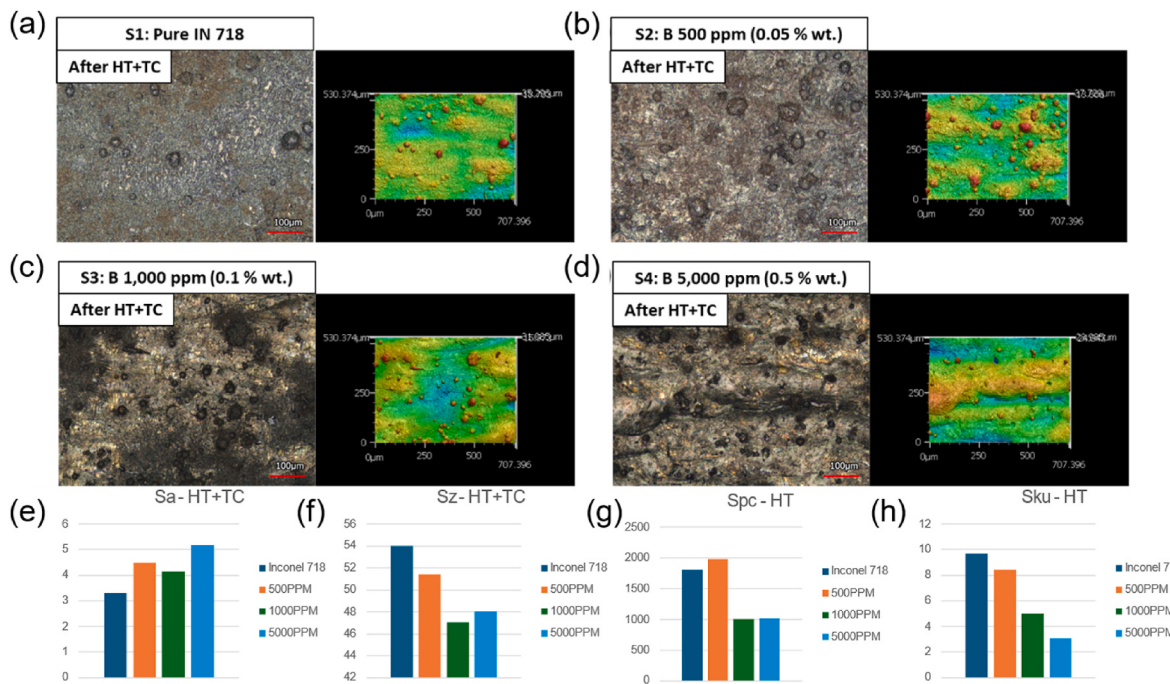


Fig. 11. Surface characteristics of samples after heat treatment (HT) and thermal cycling (TC).

Inconel 718 when introduced in low concentrations. This refinement contributes to a more uniform surface finish, which in turn affects optical behavior. A smoother surface typically reduces diffuse reflectance while increasing specular reflectivity, a characteristic that can be beneficial for applications requiring controlled light absorption. Furthermore, boron's interaction with other alloying elements may help reduce oxidation. However, it is important to note that excessive boron can lead to grain boundary segregation, potentially compromising mechanical properties such as toughness and strength, particularly in high-temperature and high-stress environments. Therefore, while boron can

enhance optical properties and oxidation resistance, its concentration must be carefully optimized to balance between performance and structural integrity.

### 3.2.4. High temperature emissivity

For high-temperature emissivity measurements at 700 °C, a Thermo Fisher iS50 FTIR spectrometer with a high-temperature stage was used. At this temperature, an integrating sphere could not be employed, so only direct-normal emissivity measurements were obtained; therefore, these results cannot be directly compared to those from the previous

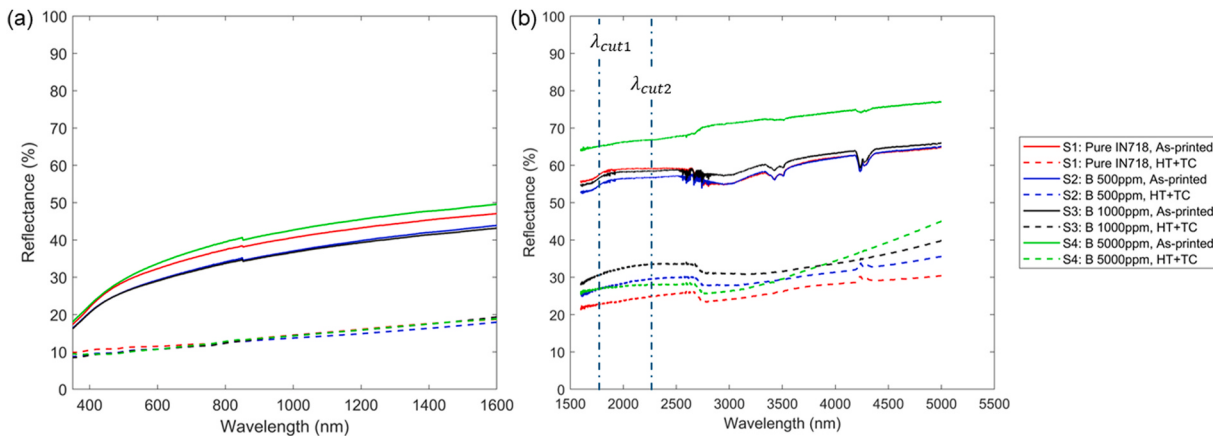


**Fig. 12.** Reflectance of samples before and after heat treatment (HT) and thermal cycling (TC) for the (a) visible light range and (b) infrared range.

section. Fig. 13 shows the emissivity as a function of wavelength at 700 °C. The spectral range was limited to 2.5–5.0 μm, since Wien's displacement law indicates that the peak of the blackbody radiation spectrum at ~973 K (700 °C) lies near 3 μm [84].

Kirchhoff's law dictates that emissivity ( $\varepsilon$ ) equals absorptivity ( $\alpha$ ) for a reciprocal material in thermal equilibrium [85,86]. In our measurements (2.5–5 μm, 700 °C), the emissivity spectra of all HT + TC samples essentially overlap, showing no significant dependence on boron content. This behavior differs from the room-temperature absorptivity trends reported in Sect. 3.2.3, where absorptivity varied systematically with composition. The uniform high-temperature emissivity suggests that surface oxidation has homogenized the radiative properties of all samples. During heating and cycling, each sample develops a thin oxide scale and increased surface roughness, and such oxidized metallic surfaces typically exhibit high, stable emissivity. As a result, all HT + TC specimens show similarly elevated emissivity values, regardless of boron content. Therefore, at 700 °C, the emissivity of the HT + TC samples is essentially independent of boron composition. The oxide-induced surface layer dominates the infrared response, overriding any compositional differences.

#### 4. Discussions about adding boron into Inconel 718 and 3D printing solar receiver tubes

##### 4.1. Mechanical properties of boron-enhanced Inconel 718 (by comparison)

The addition of boron to Inconel 718 introduces significant improvements in both mechanical and optical properties, making it a promising material for high-temperature CSP applications. By influencing the alloy's microstructure, boron enhances the strength, hardness, and thermal stability while also increasing its solar absorptivity.

One of the primary benefits of boron incorporation is its role in strengthening Inconel 718 by promoting the formation of the eutectic γ phase. This phase contributes to increased tensile strength and hardness, making the material more resistant to mechanical stress. However, the excessive formation of the eutectic γ phase induced by a large amount of boron content, led to the suppression of plastic deformation. In this study, the heat treatment method reported by Liu *et al.* [61] was adapted to segment interconnecting eutectic γ phase into a more favorable granular-shaped Laves phase. This transformation enhances ductility without compromising tensile strength, ensuring the alloy retains its structural integrity under mechanical loads. The exceptional tensile characteristics of boron-enhanced Inconel 718 were compared to reported properties of Inconel 718 with different processing techniques [80,87–90] in Fig. 14. It should be noted that the yield strength values from this study (after HT) showed high performance of boron-enhanced Inconel 718. Also, it is reasonable to expect more promising tensile strength from further optimized heat treatment methods.

Thermal cycling (TC) also plays a critical role in the long-term stability of boron-enhanced Inconel 718. While alloys with lower boron content exhibit minimal structural changes under repeated thermal exposure, higher boron concentrations promote more extensive eutectic γ phase formation, leading to increased brittleness. This suggests that while moderate boron levels improve strength and thermal stability, excessive amounts may introduce microstructural instability. The optimization of boron content, combined with appropriate heat treatment strategies, is therefore essential to ensure long-term reliability in high-temperature environments.

Another key advantage of boron addition is the substantial increase in microhardness across different processing stages, from the as-printed condition to post-heat treatment and thermal cycling. The improved hardness contributes to greater wear resistance, which is particularly beneficial in applications where materials are exposed to prolonged mechanical and thermal stress. This enhancement makes boron-enhanced Inconel 718 a more durable alternative to traditional high-temperature alloys for applications in Gen3 particle-based solar receivers.

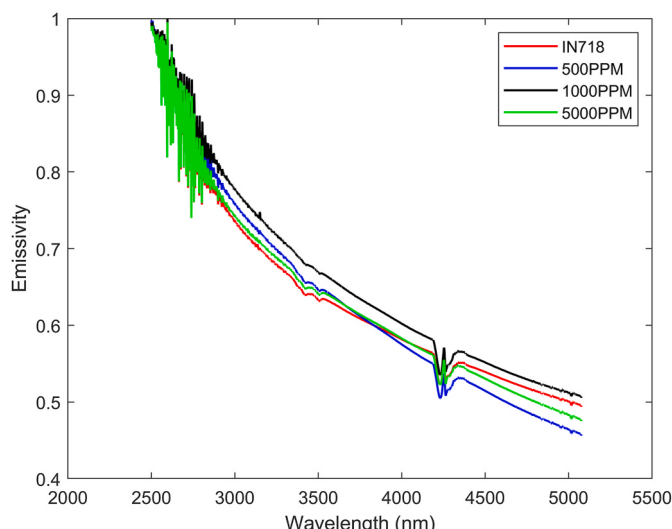


**Fig. 13.** Emissivity of heat-treated samples with thermal cycling at 700 °C between 2.5 μm and 5 μm.

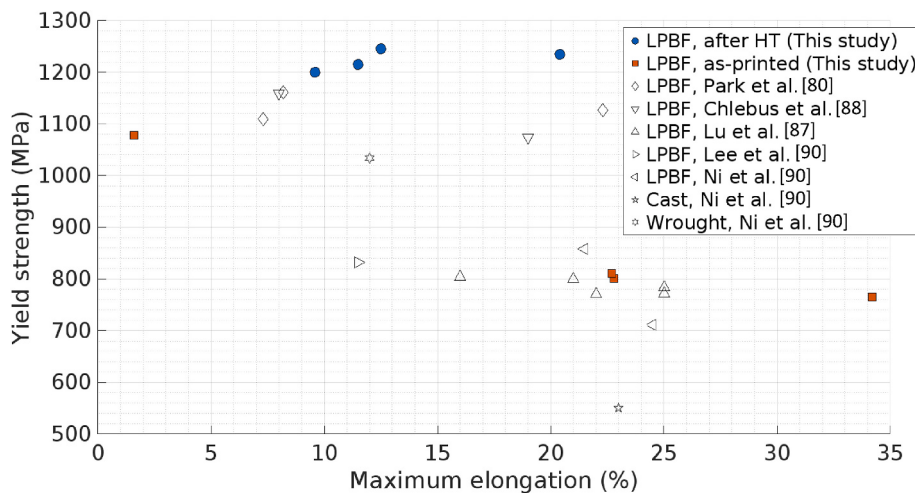


**Fig. 14.** Comparison of tensile strength and maximum elongation obtained in this work with Inconel 718 reported by references [80,87–90].

Beyond mechanical improvements, boron also enhances the optical properties of Inconel 718. The reduction in reflectivity across key wavelength ranges enhances the efficiency of solar energy absorption, which is critical for improving the performance of CSP receiver tubes. Additionally, boron's interaction with grain boundaries influences emissivity, helping to optimize thermal radiation management. Unlike conventional coatings, which degrade over time at high temperatures, boron-enhanced Inconel 718 offers a more durable and long-lasting solution for improving optical performance.

#### 4.2. 3D printing concentrated solar receiver tubes using the boron-doped Inconel 718 powders

Solar receiver tubes with internal fin structures were 3D printed using the 5000 ppm Boron-doped Inconel 718 powders on the EOS M290 Powder Bed Fusion machine, as shown in Fig. 15 (a). The fins were optimized using a Surrogate-assisted model to balance the heat transfer enhancement and the pressure loss increase [33]. A multiphysics model was developed to evaluate the thermo-hydro-mechanical performance of finned tubes when the uneven solar flux was shining on the tubes [25]. The 3D printing parameters were selected as they achieved the print without defects (e.g., cracks, delamination, uneven layer deposition) [91]. Fig. 15 (b) shows that the locking features were printed to ensure that the internal fins can be aligned with each other piece when welding the 100 mm long short sections. Eventually, a 1.5 m long receiver tube was fabricated for testing, as shown in Fig. 15 (c). We performed thermofluid experiments on a customized heat transfer test

loop to confirm the CFD-based results of fin optimization [34].

Overall, integrating boron into Inconel 718 offers a dual advantage—enhancing both mechanical strength and optical performance. By carefully controlling boron content and optimizing post-processing techniques, the alloy achieves superior tensile strength, hardness, and ductility while improving solar absorptivity and thermal stability. These advancements position boron-enhanced Inconel 718 as a strong candidate for high-temperature CSP applications.

## 5. Conclusion

This study includes a detailed characterization of a new promising candidate for the next-generation high-temperature CSP applications, Boron-enhanced Inconel 718. By tailoring the composition and microstructural characteristics, such as refining phase distribution and optimizing grain structures, the absorptivity and mechanical performance of Inconel 718 can be improved. This approach could lead to the development of more resilient and high-performance receiver tubes capable of withstanding extreme operating conditions, reducing maintenance costs, and extending the lifespan of CSP components. After a thorough analysis of the results, the following conclusions were made:

- Laser powder bed fusion achieved up to 5000 ppm of boron content, while conventional manufacturing processes can only achieve 100 ppm.
- Adding boron to Inconel 718 induced the formation of a larger amount of eutectic  $\gamma$  phase in the microstructure. While increased

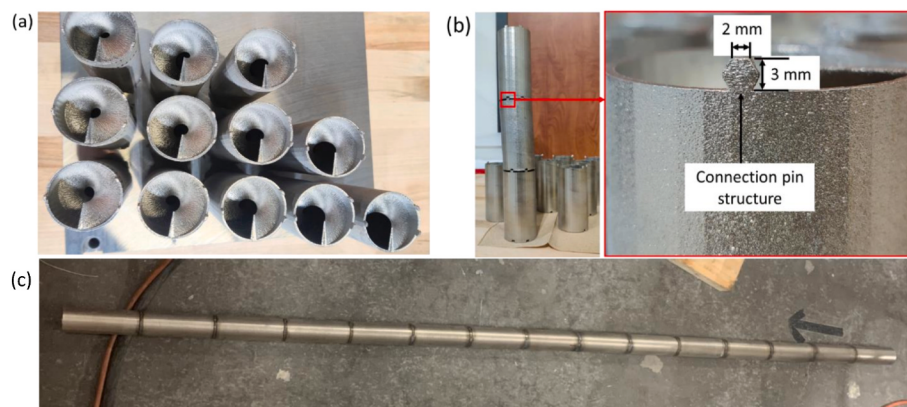


**Fig. 15.** (a) Printed solar receiver tubes with internal fin structures; (b) connection pin structure for multi-tube alignment; (c) A welded 3D printed 1.5 m long tube for heat transfer experiment [34].

boron content enhanced the tensile strength and the hardness, an excessive amount of eutectic  $\gamma$  phase suppressed the plastic deformation of the alloy.

- A granular-shaped Laves phase was formed after the HT process. Compared to the Laves phase with the long-striped shape or thick web shape, the granular-shaped Laves phase enhanced the alloy's ductility, while enhanced tensile strength was not negatively affected. The sample S3 (1000 ppm) showed an ultimate tensile strength of 1460 MPa with an elongation of 12.5 %.
- Thermal cycling (TC) promoted the formation of the eutectic  $\gamma$  phase. While samples with relatively low boron content (less than 1000 ppm) were not heavily affected by TC, the sample with the highest boron content (5000 ppm) showed severe formation of the eutectic  $\gamma$  phase.
- Boron-enhanced Inconel 718 exhibited microhardness increases up to 36.6 %, 9.2 %, and 19.0 % for as-printed, after heat treatment (HT), and after heat treatment (HT) + thermal cycling (TC), respectively.
- Boron-enhanced Inconel 718 showed improved optical properties by showing reflectance decreased by approximately 10 %.
- While this study does not increase the material absorptivity to a comparable status as Pyromark 2500, the main objective of this study is to replace the coating with another strategy to increase the longevity of the part lifetime; an in-depth techno-economic analysis would be required to determine the trade-off between the extended lifetime of the receiver tubes and decrease in Operational Expenditures is worth the lower absorptivity of the receiver tubes.

#### CRediT authorship contribution statement

**Jeongwoo Lee:** Writing – review & editing, Writing – original draft,

#### Appendix A

Methodology, Investigation, Formal analysis, Data curation. **Mathew Farias:** Writing – review & editing, Writing – original draft, Investigation, Formal analysis, Data curation. **Hernan Aparicio:** Investigation, Formal analysis. **Haomin Li:** Investigation. **Bardia Nabavi:** Investigation, Writing – review & editing. **Bo Zhao:** Writing – review & editing, Resources, Investigation, Formal analysis. **Farid Ahmed:** Writing – review & editing, Supervision, Resources, Investigation. **Peiwen Li:** Writing – review & editing, Supervision, Resources, Project administration, Investigation, Funding acquisition. **Ben Xu:** Writing – review & editing, Writing – original draft, Supervision, Software, Resources, Project administration, Methodology, Investigation, Funding acquisition, Conceptualization. **Jianzhi Li:** Writing – review & editing, Supervision, Resources, Project administration, Investigation, Funding acquisition.

#### Declaration of competing interest

The authors declare that they have no known competing financial interests or personal relationships that could have appeared to influence the work reported in this paper.

#### Acknowledgments

The authors are grateful for the support from the U.S. Department of Energy's Office of Energy Efficiency and Renewable Energy (EERE) under the Solar Energy Technologies Office (SETO) Award No. DE-EE0009380.

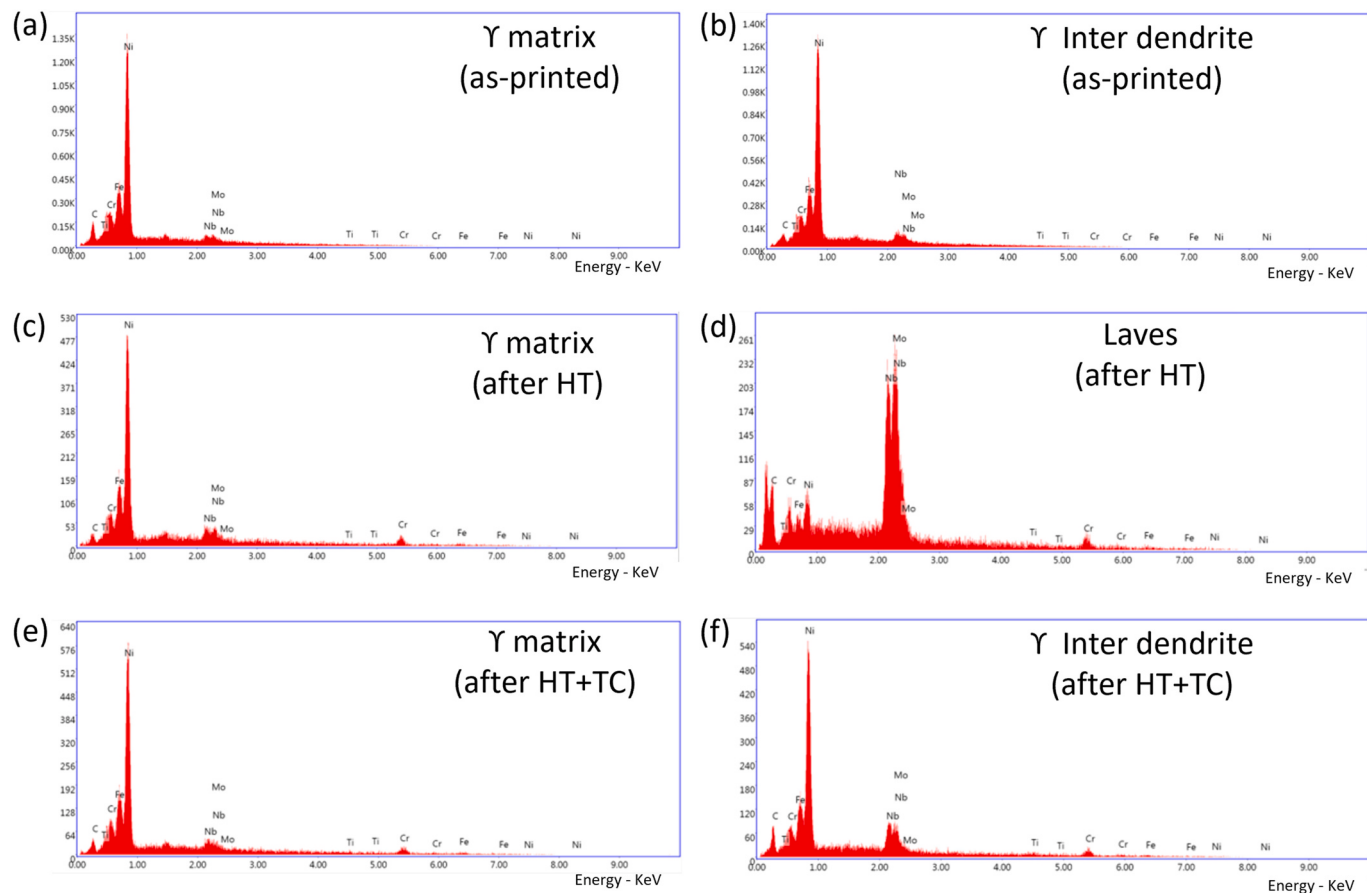


**Fig. A.1.** EDAX spectrum results of major phases in boron-enhanced Inconel 718.

**Table A.1**

EDAX analysis results of major phases in boron-enhanced Inconel 718

Elements	As-printed				After HT				After HT + TC			
	Y matrix		Y Inter dendrite		Y matrix		Laves		Y matrix		Y Inter dendrite	
	(wt. %)	(at. %)	(wt. %)	(at. %)	(wt. %)	(at. %)	(wt. %)	(at. %)	(wt. %)	(at. %)	(wt. %)	(at. %)
C	5.57	22.34	3.02	13.35	4.59	19.37	15.23	56.04	5.31	21.64	8.94	33.77
Ti	8.76	8.80	8.37	9.28	5.12	5.42	0.18	0.16	5.65	5.77	5.49	5.20
Cr	9.92	9.18	8.85	9.05	9.11	8.89	7.15	6.08	9.76	9.18	7.65	6.68
Fe	10.68	9.21	10.42	9.92	9.94	9.03	1.5	1.19	11.30	9.90	7.33	5.96
Ni	55.63	45.63	56.41	51.06	58.13	50.22	3.42	2.58	57.89	48.26	49.34	38.13
Nb	5.91	3.06	9.76	5.59	7.50	4.09	37.17	17.68	6.19	3.26	14.17	6.92
Mo	3.53	1.77	3.16	1.75	5.62	2.97	35.34	16.28	3.91	1.99	7.07	3.35

## Data availability

Data will be made available on request.

## References

- [1] M. Blanco, S. Miller, Introduction to concentrating solar thermal (CST) technologies, in: Advances in Concentrating Solar Thermal Research and Technology, Elsevier, 2017, pp. 3–25.
- [2] J. Li, Scaling up concentrating solar thermal technology in China, Renew. Sustain. Energy Rev. 13 (8) (2009) 2051–2060.
- [3] T. Eglinton, J. Hinkley, A. Beath, M. Dell'Amico, Potential applications of concentrated solar thermal technologies in the Australian minerals processing and extractive metallurgical industry, Jom 65 (12) (2013) 1710–1720.
- [4] M. Laporte-Azcué, P. González-Gómez, M.d. I.R. Rodríguez-Sánchez, D. Santana, Material selection for solar central receiver tubes, Sol. Energy Mater. Sol. Cell. 231 (2021) 111317.
- [5] G. Manzolini, G. Lucca, M. Binotti, G. Lozza, A two-step procedure for the selection of innovative high temperature heat transfer fluids in solar tower power plants, Renew. Energy 177 (2021) 807–822.
- [6] "The SunShot 2030 Goals: 3¢ per Kilowatt Hour for PV and 5¢ per Kilowatt Hour for Dispatchable CSP | Department of Energy, <https://www.energy.gov/sites/prod/files/2020/09/f79/SunShot%202030%20White%20Paper.pdf>.
- [7] Y.-L. He, et al., Perspective of concentrating solar power, Energy 198 (2020) 117373.
- [8] T.R. Mancini, J.A. Gary, G.J. Kolb, C.K. Ho, Power Tower Technology Roadmap and Cost Reduction Plan, Sandia National Laboratories (SNL), Albuquerque, NM, and Livermore, CA, 2011.
- [9] A. International Renewable Energy, Renewable Energy Technologies: Cost Analysis Series, vol. 1, International Renewable Energy Agency (IRENA), 2012, p. 274.

- [10] C. Singer, R. Buck, R. Pitz-Paal, H. Müller-Steinhagen, Assessment of Solar Power Tower Driven Ultrasupercritical Steam Cycles Applying Tubular Central Receivers with Varied Heat Transfer Media, 2010.
- [11] C. Chang, X. Li, Q.Q. Zhang, Experimental and numerical study of the heat transfer characteristics in solar thermal absorber tubes with circumferentially non-uniform heat flux, *Energy Proc.* 49 (2014) 305–313.
- [12] C.K. Ho, B.D. Iverson, Review of high-temperature central receiver designs for concentrating solar power, *Renew. Sustain. Energy Rev.* 29 (2014) 835–846.
- [13] M.H. Abedini-Sanigy, F. Ahmadi, E. Goshtasbirad, M. Yaghoubi, Thermal stress analysis of absorber tube for a parabolic collector under quasi-steady state condition, *Energy Proc.* 69 (2015) 3–13.
- [14] S. Khanna, S.B. Kedare, S. Singh, Deflection and stresses in absorber tube of solar parabolic trough due to circumferential and axial flux variations on absorber tube supported at multiple points, *Sol. Energy* 99 (2014) 134–151.
- [15] F. Tancre, et al., Design of a creep resistant nickel base superalloy for power plant applications: Part 3-Experimental results, *Mater. Sci. Technol.* 19 (3) (2003) 296–302.
- [16] A.M. Kruizenga, D.D. Gill, M.E. LaFord, Corrosion of high temperature alloys in solar salt at 400, 500, and 680°C. Sandia National Lab., SNL-CA), Livermore, CA (United States), 2013.
- [17] Design documentation of a steel receiver at solar Power plant, <https://allcons.cz/en/reference/design-documentation-of-a-steel-receiver-at-solar-power-plant/>.
- [18] S. Hatcher, R. Khadka, B. Pidaparthi, S. Misssoum, P. Li, B. Xu, Numerical Study of Solar Receiver Tube for Enhanced Thermal Efficiency and Durability in Concentrated Solar Power Tower Plant, 85772, American Society of Mechanical Engineers, 2022 V001T05A002.
- [19] M. Laporte-Azcué, P.A. González-Gómez, M.d. I.R. Rodríguez-Sánchez, D. Santana, Deflection and stresses in solar central receivers, *Sol. Energy* 195 (2020) 355–368.
- [20] A. Morales, G. San Vicente, A new generation of absorber tubes for concentrating solar thermal (CST) systems. Advances in Concentrating Solar Thermal Research and Technology, 2017, pp. 59–73.
- [21] M. Sarvghad, S.D. Maher, D. Collard, M. Tassan, G. Will, T.A. Steinberg, Materials compatibility for the next generation of Concentrated Solar Power plants, *Energy Storage Mater.* 14 (2018) 179–198.
- [22] K.L. Murty, I. Charit, Structural materials for Gen-IV nuclear reactors: challenges and opportunities, *J. Nucl. Mater.* 383 (1–2) (2008) 189–195.
- [23] S. Du, Z. Wang, S. Shen, Thermal and structural evaluation of composite solar receiver tubes for Gen3 concentrated solar power systems, *Renew. Energy* 189 (2022) 117–128.
- [24] J.D. Ortega, J.M. Christian, C.K. Ho, Design and Testing of a Novel Bladed Receiver, 57595, American Society of Mechanical Engineers, 2017 V001T05A007.
- [25] S. Hatcher, M. Farias, J. Li, P. Li, B. Xu, Numerical Study of Solar Receiver Tube with Modified Surface Roughness for Enhanced and Selective Absorptivity in Concentrated Solar Power Tower, 87189, American Society of Mechanical Engineers, 2023 V001T05A002.
- [26] M. Cantone, M. Cagnoli, J.F. Reche, L. Savoldi, One-side heating test and modeling of tubular receivers equipped with turbulence promoters for solar tower applications, *Appl. Energy* 277 (2020) 115519.
- [27] M. Laporte-Azcué, M.R. Rodríguez-Sánchez, Thermal efficiency and endurance enhancement of tubular solar receivers using functionally graded materials, *Appl. Energy* 360 (2024) 122842.
- [28] R. Mochahari, A.K. Ray, K.R. Kumar, D. Rakshit, Thermal performance of a supercritical CO<sub>2</sub> based central receiver, *Mater. Today Proc.* 90 (2023) 56–60.
- [29] M. Wei, Y. Fan, L. Luo, G. Flamant, Design and optimization of baffled fluid distributor for realizing target flow distribution in a tubular solar receiver, *Energy* 136 (2017) 126–134.
- [30] M. Laporte-Azcué, P.A. González-Gómez, D. Santana, Solar receiver endurance assessment under non-conventional operation modes, *Renew. Energy* 231 (2024) 120939.
- [31] M. Mehos, et al., Concentrating Solar Power Gen3 Demonstration Roadmap, National Renewable Energy Lab.(NREL), Golden, CO (United States), 2017.
- [32] Y.-L. He, K. Wang, Y. Qiu, B.-C. Du, Q. Liang, S. Du, Review of the solar flux distribution in concentrated solar power: non-uniform features, challenges, and solutions, *Appl. Therm. Eng.* 149 (2019) 448–474.
- [33] B. Pidaparthi, S. Misssoum, B. Xu, P. Li, Helical fins for concentrated solar receivers: design optimization and entropy analysis, *J. Energy Resour. Technol.* 145 (12) (2023) 121706.
- [34] F. Haddad, et al., Flow and heat transfer experimental study for 3D-printed solar receiving tubes with helical fins at internal surface, *J. Sol. Energy Eng.* 147 (1) (2025).
- [35] M.L. Köhler, J. Kunz, S. Herzog, A. Kaletsch, C. Broeckmann, Microstructure analysis of novel LPBF-processed duplex stainless steels correlated to their mechanical and corrosion properties, *Mater. Sci. Eng., A* 801 (2021) 140432.
- [36] J. Lee, A. Parmar, Y.C. Shin, L. Zhu, Enhanced magnetic properties and Goss texture development of FeSi3.5 by direct energy deposition, *J. Mater. Sci.* 59 (31) (2024) 14510–14529.
- [37] J. Lee, Y.C. Shin, Effects of composition and post heat treatment on shape memory characteristics and mechanical properties for laser direct deposited nitinol, *Lasers in Manufacturing and Materials Processing* 6 (2019) 41–58.
- [38] J. Lee, S. Akin, J.R. Walsh, M.B.G. Jun, H. Lee, Y.C. Shin, A Nitinol structure with functionally gradient pure titanium layers and hydroxyapatite over-coating for orthopedic implant applications, *Prog. Additiv. Manufac.* 9 (4) (2024) 1025–1038.
- [39] J. Lee, STUDY ON CHARACTERISTICS OF DIRECT ENERGY DEPOSITED NITINOL AND A NOVEL COATING METHOD FOR ORTHOPEDIC IMPLANT APPLICATIONS, 2022.
- [40] M. Simonelli, et al., A comparison of Ti-6Al-4V in-situ alloying in Selective Laser Melting using simply-mixed and satellited powder blend feedstocks, *Mater. Char.* 143 (2018) 118–126.
- [41] L.-L. Xing, C.-C. Zhao, H. Chen, Z.-J. Shen, W. Liu, Microstructure of a Ti-50 wt% Ta alloy produced via laser powder bed fusion, *Acta Metall. Sin.* 33 (2020) 981–990.
- [42] A. El Hassanin, F. Scherillo, U. Prisco, R. Sansone, A. Astarita, Selective laser melting of Cu-inconel 718 powder mixtures, *J. Manuf. Process.* 59 (2020) 679–689.
- [43] Y. Wen, et al., Laser powder bed fusion of compositionally graded CoCrMo-Inconel 718, *Addit. Manuf.* 40 (2021) 101926.
- [44] J.A. Glerum, C. Kenel, T. Sun, D.C. Dunand, Synthesis of precipitation-strengthened Al-Sc, Al-Zr and Al-Sc-Zr alloys via selective laser melting of elemental powder blends, *Addit. Manuf.* 36 (2020) 101461.
- [45] N. Kang, P. Coddet, L. Dembinski, H. Liao, C. Coddet, Microstructure and strength analysis of eutectic Al-Si alloy in-situ manufactured using selective laser melting from elemental powder mixture, *J. Alloys Compd.* 691 (2017) 316–322.
- [46] Q. Zhong, K. Wei, X. Yue, R. Zhou, X. Zeng, Powder densification behavior and microstructure formation mechanism of W-Ni alloy processed by selective laser melting, *J. Alloys Compd.* 908 (2022) 164609.
- [47] J. Lee, Y.C. Shin, Crack-free tungsten coating on ODS plate via a modified laser-based additive technique: offset laser cladding, *Surf. Coating. Technol.* 476 (2024) 130285.
- [48] P. Chen, S. Li, Y. Zhou, M. Yan, M.M. Attallah, Fabricating CoCrFeMnNi high entropy alloy via selective laser melting in-situ alloying, *J. Mater. Sci. Technol.* 43 (2020) 40–43.
- [49] Y. Hou, H. Su, H. Zhang, X. Wang, C. Wang, Fabricating homogeneous FeCoCrNi high-entropy alloys via SLM in situ alloying, *Metals* 11 (6) (2021) 942.
- [50] F. Zhang, et al., Composition fine-tuning for directed energy deposition of Ti-6Al-4V, *J. Mater. Process. Technol.* 299 (2022) 117321.
- [51] F. Caiazzo, V. Alfieri, G. Corrado, P. Argenio, Laser powder-bed fusion of Inconel 718 to manufacture turbine blades, *Int. J. Adv. Des. Manuf. Technol.* 93 (2017) 4023–4031.
- [52] A. Hilaire, E. Andrieu, X. Wu, High-temperature mechanical properties of alloy 718 produced by laser powder bed fusion with different processing parameters, *Addit. Manuf.* 26 (2019) 147–160.
- [53] X. Li, M. Ou, M. Wang, L. Zhang, Y. Ma, K. Liu, Effect of boron addition on the microstructure and mechanical properties of K4750 nickel-based superalloy, *J. Mater. Sci. Technol.* 60 (2021) 177–185.
- [54] C. Wang, Y. Guo, J. Guo, L. Zhou, Microstructural stability and mechanical properties of a boron modified Ni-Fe based superalloy for steam boiler applications, *Mater. Sci. Eng., A* 639 (2015) 380–388.
- [55] Y. Liu, K.Y. Chen, G. Lu, J.H. Zhang, Z.Q. Hu, Impurity effects on the NiNi3Al interface cohesion, *Acta Mater.* 45 (5) (1997) 1837–1849.
- [56] P.J. Zhou, J.J. Yu, X.F. Sun, H.R. Guan, Z.Q. Hu, The role of boron on a conventional nickel-based superalloy, *Mater. Sci. Eng., A* 491 (1–2) (2008) 159–163.
- [57] W. Xm, H. Xl, Effect of boron addition on structure and properties of low carbon bainitic steels, *ISIJ Int.* 42 (Suppl) (2002) S38–S46.
- [58] B.C. Yan, J. Zhang, L.H. Lou, Effect of boron additions on the microstructure and transverse properties of a directionally solidified superalloy, *Mater. Sci. Eng., A* 474 (1–2) (2008) 39–47.
- [59] L. Xiao, M.C. Chaturvedi, D.L. Chen, Effect of boron on the low-cycle fatigue behavior and deformation structure of INCONEL 718 at 650 C, *Metall. Mater. Trans. 35* (2004) 3477–3487.
- [60] L. Xiao, M.C. Chaturvedi, D.L. Chen, Low-cycle fatigue behavior of INCONEL 718 superalloy with different concentrations of boron at room temperature, *Metall. Mater. Trans. 36* (2005) 2671–2684.
- [61] F. Liu, F. Lyu, F. Liu, X. Lin, C. Huang, Laves phase control of inconel 718 superalloy fabricated by laser direct energy deposition via δ aging and solution treatment, *J. Mater. Res. Technol.* 9 (5) (2020) 9753–9765.
- [62] B. Nabavi, S. Jafari Ghalekohneh, K.J. Shayegan, E.J. Tervo, H. Atwater, B. Zhao, High-temperature strong nonreciprocal thermal radiation from semiconductors, *ACS Photonics* (2025/04/30 2025), <https://doi.org/10.1021/acspophotonics.5c00365>.
- [63] W.M. Tucho, P. Cuvillier, A. Sjolyst-Kverneland, V. Hansen, Microstructure and hardness studies of Inconel 718 manufactured by selective laser melting before and after solution heat treatment, *Mater. Sci. Eng., A* 689 (2017) 220–232.
- [64] L.L. Parimi, G.A. Ravi, D. Clark, M.M. Attallah, Microstructural and texture development in direct laser fabricated IN718, *Mater. Char.* 89 (2014) 102–111.
- [65] E. Hosseini, V.A. Popovich, A review of mechanical properties of additively manufactured Inconel 718, *Addit. Manuf.* 30 (2019) 100877.
- [66] F. Liu, et al., Microstructural changes in a laser solid forming Inconel 718 superalloy thin wall in the deposition direction, *Opt. Laser. Technol.* 45 (2013) 330–335.
- [67] H. Qi, M. Azer, A. Ritter, Studies of standard heat treatment effects on microstructure and mechanical properties of laser net shape manufactured Inconel 718, *Metall. Mater. Trans. 40* (2009) 2410–2422.
- [68] R.J. Vikram, A. Singh, S. Suwas, Effect of heat treatment on the modification of microstructure of selective laser melted (SLM) IN718 and its consequences on mechanical behavior, *J. Mater. Res. Technol.* 35 (15) (2020) 1949–1962.
- [69] Y. Xu, Y. Gong, P. Li, Y. Yang, Y. Qi, The effect of laser power on the microstructure and wear performance of IN718 superalloy fabricated by laser additive manufacturing, *Int. J. Adv. Des. Manuf. Technol.* 108 (2020) 2245–2254.
- [70] Y. Kaynak, E. Tascioglu, Post-processing effects on the surface characteristics of Inconel 718 alloy fabricated by selective laser melting additive manufacturing, *Progress in Additive Manufacturing* 5 (2) (2020) 221–234.

- [71] G.H. Cao, et al., Investigations of  $\gamma'$ ,  $\gamma''$  and  $\delta$  precipitates in heat-treated Inconel 718 alloy fabricated by selective laser melting, *Mater. Char.* 136 (2018) 398–406.
- [72] K. Gruber, R. Dziedzic, B. Kuźnicka, B. Madejski, M. Malicki, Impact of high temperature stress relieving on final properties of Inconel 718 processed by laser powder bed fusion, *Mater. Sci. Eng., A* 813 (2021) 141111.
- [73] S. Ghaemifar, H. Mirzadeh, Precipitation kinetics of niobium carbide (NbC) during homogenization heat treatment of additively manufactured inconel 718 superalloy, *J. Mater. Res. Technol.* 25 (2023) 1774–1781.
- [74] K.N. Amato, et al., Microstructures and mechanical behavior of Inconel 718 fabricated by selective laser melting, *Acta Mater.* 60 (5) (2012) 2229–2239.
- [75] R. Lawitzki, et al., Differentiation of  $\gamma'$ -and  $\gamma''$ -precipitates in Inconel 718 by a complementary study with small-angle neutron scattering and analytical microscopy, *Acta Mater.* 163 (2019) 28–39.
- [76] K. Kunze, T. Etter, J. Grässlin, V. Shklover, Texture, anisotropy in microstructure and mechanical properties of IN738LC alloy processed by selective laser melting (SLM), *Mater. Sci. Eng., A* 620 (2015) 213–222.
- [77] S. Raghavan, et al., Effect of different heat treatments on the microstructure and mechanical properties in selective laser melted INCONEL 718 alloy, *Mater. Manuf. Process.* 32 (14) (2017) 1588–1595.
- [78] G.D.J. Ram, A.V. Reddy, K.P. Rao, G.M. Reddy, Microstructure and mechanical properties of Inconel 718 electron beam welds, *Mater. Sci. Technol.* 21 (10) (2005) 1132–1138.
- [79] S. Sui, et al., The influence of Laves phases on the room temperature tensile properties of Inconel 718 fabricated by powder feeding laser additive manufacturing, *Acta Mater.* 164 (2019) 413–427.
- [80] S.Y. Park, K.S. Kim, M.C. Kim, M.E. Kassner, K.A. Lee, Effect of post-heat treatment on the tensile and cryogenic impact toughness properties of inconel 718 manufactured by selective laser melting, *Adv. Eng. Mater.* 23 (3) (2021) 2001005.
- [81] J.F.S. Markanday, et al., Occurrence of a brass texture and elastic anisotropy in laser blown powder processed superalloy IN718, *Mater. Sci. Eng., A* 825 (2021) 141781.
- [82] K.C.G. Candioto, F.R. Caliari, D.A.P. Reis, A.A. Couto, C.A. Nunes, Characterization of the superalloy Inconel 718 after double aging heat treatment. Mechanical and Materials Engineering of Modern Structure and Component Design, 2015, pp. 293–300.
- [83] K. Burlafinger, A. Vetter, C.J. Brabec, Maximizing concentrated solar power (CSP) plant overall efficiencies by using spectral selective absorbers at optimal operation temperatures, *Sol. Energy* 120 (2015) 428–438.
- [84] M. Habibi, S.C. Yelishala, Y. Zhu, E.J. Tervo, M.A. Steiner, L. Cui, Enhanced power density in zero-vacuum-gap thermophotovoltaic devices, *Energy Environ. Sci.* 18 (2025) 1514–1523.
- [85] G.A. Greene, C.C. Finfrock, T.F. Irvine Jr, Total hemispherical emissivity of oxidized Inconel 718 in the temperature range 300–1000 C, *Exp. Therm. Fluid Sci.* 22 (3–4) (2000) 145–153.
- [86] M. Balat-Pichelin, J.L. Sans, E. Béche, L. Charpentier, A. Ferrière, S. Chomette, Emissivity at high temperature of Ni-based superalloys for the design of solar receivers for future tower power plants, *Sol. Energy Mater. Sol. Cell.* 227 (2021) 111066.
- [87] E. Chlebus, K. Gruber, B. Kuźnicka, J. Kurzak, T. Kurzynowski, Effect of heat treatment on the microstructure and mechanical properties of Inconel 718 processed by selective laser melting, *Mater. Sci. Eng., A* 639 (2015) 647–655.
- [88] Y. Lu, et al., Study on the microstructure, mechanical property and residual stress of SLM Inconel-718 alloy manufactured by differing island scanning strategy, *Opt. Laser. Technol.* 75 (2015) 197–206.
- [89] J. Lee, et al., Correlation between microstructure and tensile properties of STS 316L and Inconel 718 fabricated by selective laser melting (SLM), *J. Nanosci. Nanotechnol.* 20 (11) (2020) 6807–6814.
- [90] M. Ni, et al., Anisotropic tensile behavior of in situ precipitation strengthened Inconel 718 fabricated by additive manufacturing, *Mater. Sci. Eng., A* 701 (2017) 344–351.
- [91] B. Xu, 3D printing of solar absorber tube with internal/external structures for heat transfer enhancement and temperature leveling using additive manufacturing technology (No. Final report: DOE-MSU-1), Mississippi State Univ., Starkville, MS (United States) (2021).